An Analytical Model for Solar Energy Reflected from Space with Selected Applications

Onur Çelik[a,*], Colin McInnes[a]

[a]*James Watt School of Engineering, University of Glasgow, Glasgow G12 8QQ, Scotland, United Kingdom*

Abstract

Orbiting solar reflectors can be employed to redirect incoming sunlight to provide/reject additional solar energy to/from a planetary body. The concept has been studied in the past for a variety of applications, among which enhancing terrestrial solar power generation, supporting lunar exploration and terraforming Mars are the most prominent. Despite the potential of the concept, previous studies have assumed a perfect reflector, and have only relied on simplified geometric analyses to calculate the quantity of energy delivered with minimal consideration of geometric and physical losses. In this paper, an analytical model is developed for a reflector in a circular orbit to calculate the total energy delivered to a stationary ground-target, such as a solar power farm. A perfectly ideal flat reflector is also assumed to avoid material specific considerations but atmospheric transmission losses, fixed ground-target size and solar panel orientation are included. Case studies demonstrate the significance of high-fidelity modelling, provide new insights into the scalability of the results to test the effectiveness of the concept at different solar system objects including delivering solar energy at the Earth, Moon and Mars.

Keywords: orbiting solar reflectors, space-based solar energy, mathematical modelling, solar system applications

Nomenclature

A	=	area, km^2
a	=	semi-major axis of solar image, km
b	=	semi-minor axis of solar image, km
c	=	empirical parameter
D	=	diameter, km
d	=	slant range, km
E	=	energy, GWh
h	=	altitude, km
I	=	solar intensity, GW/km^2
k	=	empirical parameter
P	=	power, GW

*Corresponding author

Email addresses: `Onur.Celik@glasgow.ac.uk` (Onur Çelik), `Colin.McInnes@glasgow.ac.uk` (Colin McInnes)

R	=	radius, km
r	=	radius, km
q	=	generic parameter
T	=	orbit period, sec
t	=	time, sec
u	=	polar angle, rad
x, y	=	cartesian coordinates
α	=	angle subtended by the Sun, rad
β	=	half of central angle, rad
γ	=	instantaneous angle during orbital pass, rad
δ	=	tilt angle, rad
ϵ	=	elevation angle, rad
κ	=	scaling coefficient
μ	=	gravitational parameter, km^3/s^2
ω	=	orbital angular rate, rad/s
ψ	=	angle between incoming and outgoing sunlight, rad
ϕ	=	generic angle
ρ	=	distance to the Sun, AU
σ	=	power density, GW/km^2
τ	=	atmospheric transmission efficiency
θ	=	generic angle

Subscripts

a	=	semimajor axis
b	=	semiminor axis
E	=	Earth
el	=	elevation
im	=	image
lim	=	limit
lx	=	lux
M	=	reflector/mirror
o	=	orbit
$pass$	=	orbital pass
sf	=	solar farm/ground target
sun	=	Sun

Superscripts

0	=	beginning; first
$circ$	=	circle
eff	=	effective
ell	=	ellipse
f	=	end; last

1. Introduction

Orbiting solar reflectors are mirrors that can be utilised to redirect sunlight to a planetary body or back to space, either to input or to reject additional solar energy. Such reflectors have been

of interest for night-time illumination and other solar energy related applications even before the modern space era (Oberth, 1929). The idea had a considerable traction from the late 1960s through the beginning of the 1980s, and a number of studies have been performed to assess the feasibility of orbiting solar reflectors for terrestrial electricity generation (Buckingham & Watson, 1968; Billman et al., 1977; Ehricke, 1979), night-time illumination (Rush, 1977; Canady & Allen, 1982) and agricultural and climate applications (Ehricke, 1979). However, some of these applications anticipated falling launch costs through regular space shuttle flights, which never materialised. Further attempts to demonstrate the effectiveness of orbiting solar reflectors in the early 1990s have also been discontinued (Leary, 1993). With the growing interest towards renewable energy, commercialisation of launch services, as well as advances in on-orbit fabrication, the concept of orbiting solar reflectors has been revisited in the 21st century (Potter & Davis, 2009; Fraas, 2012; Fraas et al., 2013; Lior, 2013; Bonetti & McInnes, 2019). Recent studies primarily focus on extending the utilisation hours of terrestrial solar energy in the critical dawn/dusk period, where demand is high but supply is limited or non-existent, due to the low elevation of the Sun (Fraas, 2012; Fraas et al., 2013). Employment of orbiting solar reflectors on appropriate orbits, such that they regularly visit terrestrial solar farms, would help offset the shortfall of solar energy supply and address one of the drawbacks of terrestrial solar energy, i.e. daylight only limitation. Furthermore, orbiting solar reflectors have also been proposed for a variety of other applications at the Moon and Mars, e.g. to supplement the power requirements of a potential human outpost and long-term applications such as Mars climate engineering (Bewick et al., 2011; Gillespie et al., 2020; McInnes, 2009).

However, despite the promise, and nearly a century-old history of the orbiting solar reflector concept, previous work has relied on simplified algebraic expressions to calculate the energy delivered to a ground target. Ignoring the full dynamics of the orbital pass, the solar energy delivered has previously been calculated at the zenith point, and the results extrapolated with minimal consideration of losses due to the fixed ground target size, orientation and atmospheric transmission losses during the reflector's orbital pass. In Canady & Allen (1982), the authors used the entire reflected solar image for illumination purposes and considered energy transfer at the zenith point only, despite the geometric losses during an orbital pass. The authors then added fixed physical loss coefficients to account for atmospheric losses, reflectance and reflector wrinkling but did not account for geometric losses (Canady & Allen, 1982). In Fraas (2012), the authors attempted to implement the geometric losses in a simplified calculation without the physical losses due to atmospheric transmission (Fraas, 2012). This latter work also ignored the effect of fixed ground target area and solar panel orientation which are imperative for more accurate calculations of the quantity of the energy delivered to a solar farm (Fraas, 2012). Even though Bonetti & McInnes (2019) presented more accurate modelling, they did not provide detailed analytical insights into the various aspects of solar energy delivery to a ground target (Bonetti & McInnes, 2019).

In this paper, an analytical model of the energy delivered through reflected sunlight to a stationary ground target is presented. The main assumptions are that the reflector is in a polar or near-polar circular orbit in the dawn/dusk terminator region and a direct overhead pass is considered. The former assumption means that the reflector has a fixed pitch angle relative to the Sun, which simplifies the final integral expression of the energy delivered, but does not discount its relevance for solar energy applications. Moreover, the reflector is assumed ideal, i.e., flat and perfectly reflecting, to avoid material-specific considerations. However, the analysis will capture the full time-varying geometry of the energy transfer process, including the losses due to atmospheric transmission. Furthermore, the results are expanded to other solar system bodies and the scalability

aspects of the problem are discussed.

The paper begins by providing the basic geometric relationships relevant to determining the reflected solar image size in Sec. II. After presenting the ideal form of an energy integral and its closed-form solution in Sec. III, the impact of fixed ground-target area, ground-target orientation and time-dependent atmospheric transmission efficiency due to the motion of the reflector are implemented in the model. In Sec. IV, case studies are presented for various terrestrial and solar system applications. Conclusions and the implications of the results are presented in the final section of the paper.

2. Geometry of the solar image

The geometry between a reflector in orbit and a ground target during an orbital pass is illustrated in Figure 1.
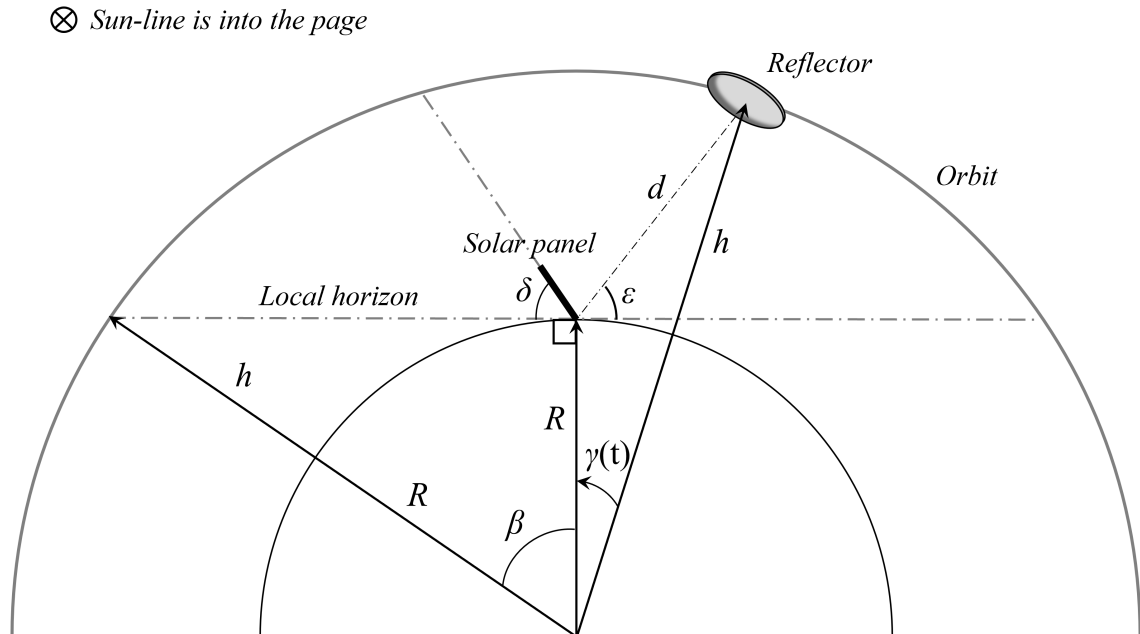

Figure 1: Geometry during an orbital pass. Image not to scale. Sun-line is into the page. During the orbital pass in a dawn/dusk orbit, the reflector is pitched at a fixed angle relative to the Sun, such that it reflects the incoming sunlight towards the planetary body.

The reflector will first rise above the horizon of the ground target at the point where a line extended in the local horizontal plane of the ground target intersects the orbit, as shown in Fig. 1. Another point symmetric with respect to the ground target defines the point where contact with the ground target ceases. Two lines extended from the center of the planetary body to these intersection points, defining an angle, denoted as 2β, which the reflector covers during its pass over the ground target. Because the pass is symmetric from rise to zenith, and zenith to set, β can be found by using the trigonometric relationships as follows:

$$\beta = \arccos \frac{R}{R+h} \tag{1}$$

4

The pass duration, T_{pass}, will then be the time it takes for the reflector to cover the angle 2β, which is a fraction of the orbit period. First the period of a circular Keplerian orbit is calculated as follows:

$$T = 2\pi\sqrt{\frac{(R+h)^3}{\mu}} \tag{2}$$

where μ denotes the gravitational parameter, R is the average radius of the planetary body and h is the orbit altitude from the surface. Then, pass duration can be expressed as

$$T_{pass} = \frac{2\beta T}{2\pi} = \frac{T}{\pi}\arccos\frac{R}{R+h} \tag{3}$$

so that T_{pass} is the time during which solar energy can be delivered to the ground target. During this time, the size and shape the solar image reflected on the ground will vary depending on the reflector's location in the sky with respect to the ground target. The image will have the shape of an ellipse at the beginning of a pass and will gradually circularise until the reflector is exactly above the ground target halfway through its pass, before stretching back to an ellipse. The exact shape of the image is determined by the elevation and an associated slant range d of the reflector from the ground target, as shown in Figure 1. If the angle between the line connecting the centre of the planetary body to the reflector and the line connecting the centre of the planetary body to the ground target at a given time is $\gamma \in [-\beta, \beta]$, the slant range d can be found as:

$$d = \sqrt{R^2 + (R+h)^2 - 2R(R+h)\cos\gamma(t)} \tag{4}$$

Moreover, since the rate of change of γ is equal to the orbit angular rate $\omega_o = \frac{2\pi}{T}$, it can also be written as $\gamma(t) = \omega_o t - \beta$, where at $t = 0$, $\gamma(0) = -\beta$ and $t = T_{pass}$, $\gamma(T_{pass}) = \beta$. One can confirm then from the geometry in Fig. 1 and from Eq. 4 that halfway through the pass, $\gamma = 0$ and $d = h$.

As the reflector sweeps an angle 2β, it also covers π radians of elevation, ϵ, from rise to set with respect to the ground target. From the triangle that the semi-major axis, the slant range and the radius of planetary body form in Fig. 1, a relationship can be written to express the elevation angle as a function of time by using the sine law:

$$\frac{R+h}{\sin(\pi/2 + \epsilon(t))} = \frac{d(t)}{\sin(\omega_o t - \beta)}$$
$$\Rightarrow \epsilon(t) = \arccos\frac{(R+h)\sin(\omega_o t - \beta)}{d(t)} \tag{5}$$

If the orbital altitude is high enough, such that the rate of elevation change is slow, the rate at which the elevation angle changes can also be written as

$$\omega_{el} = \frac{\pi}{T_{pass}} = \frac{\pi}{\frac{2\beta T}{2\pi}} = \frac{\pi\omega_o}{2\beta} \tag{6}$$

The elevation angle as a function of time can then be written as:

$$\epsilon(t) = \omega_{el}t = \frac{\pi\omega_o}{2\beta}t \tag{7}$$

The difference between the two elevation angle expressions in Eq. 5 and 6 is that the former changes with a variable angular rate whereas the latter changes at a constant angular rate.

5

Figure 2: Geometry of the reflected image (adapted from (Canady & Allen, 1982)). Orbital motion is into the page. Larger image shows the general appearance of the reflected solar image when the finite size of the reflector is included in the size of the solar image on ground. The insert shows the geometry of the reflected solar image when the reflector is assumed point-like, which is the case in this study. The assumption of fixed pitch angle is also considered in the point-like mirror.

The validity of the constant rate elevation angle approximation must be tested according to the application considered.

Then, from the geometry provided in Fig. 2, the semi-major axis a and semi-minor b of the solar image on the ground can be written as follows:

$$b(t) = d(t) \tan(\alpha/2) \tag{8a}$$

$$a(t) = \frac{b(t)}{\sin \epsilon(t)} \tag{8b}$$

where α is the angle subtended by the Sun and calculated according to Fig. 2 as follows:

$$\alpha = 2 \arctan \frac{R_{sun} - R}{\rho_{sun}} \tag{9}$$

where R_{sun} denotes the radius of the Sun, i.e., 696500 km (Giorgini, 2015), and ρ_{sun} denotes the distance from the Sun. According to Eq. 9, α is equal to 0.0093 radians at the mean Earth distance from the Sun, i.e. 1 Astronomical Unit (AU).

At this stage, it is helpful to make use of the trigonometric relationship $\sin(\arccos \theta) = \sqrt{1 - \theta^2}$

to rewrite $\sin \epsilon(t)$ as

$$\sin \epsilon(t) = \sqrt{1 - \left(\frac{(R+h)\sin(\omega_o t - \beta)}{d(t)}\right)^2}$$

$$= \sqrt{\frac{R^2 - 2R(R+h)\cos(\omega_o t - \beta) - (R+h)^2(1 - \sin(\omega_o t - \beta)^2)}{d(t)^2}} \qquad (10)$$

$$= \sqrt{\frac{(R - (R+h)\cos(\omega_o t - \beta))^2}{d(t)^2}}$$

$$= \pm \frac{R - (R+h)\cos(\omega_o t - \beta)}{d(t)}$$

As the length must be a positive value, after evaluating the outputs of Eq. 10 in Eq. 8b, the appropriate $\sin \epsilon(t)$ expression would then be:

$$\sin \epsilon(t) = \frac{(R+h)\cos(\omega_o t - \beta) - R}{d(t)} \qquad (11)$$

Then, $a(t)$ in Eq. 8 can also be rewritten as

$$a(t) = \frac{d(t)^2 \tan(\alpha/2)}{(R+h)\cos(\omega_o t - \beta) - R} \qquad (12)$$

One may notice from the analysis that the image semi-major axis a is stretched to infinity at the instant the spacecraft rises (and sets) at the horizon since the elevation angle $\epsilon = 0$ (and π) and becomes equal to b at the zenith ($\epsilon = \pi/2$), i.e. the solar image becomes circular. Then, finally, the area of the solar image, A_{im} is written as (Canady & Allen, 1982):

$$A_{im}(t) = \pi a(t)b(t) = \pi \frac{[d(t)\tan(\alpha/2)]^2}{\sin \epsilon(t)} \qquad (13)$$

from Eq. 8 and by substituting Eq. 11 into Eq. 13, the image area yields

$$A_{im}(t) = \frac{\pi d(t)^3 \tan(\alpha/2)^2}{(R+h)\cos(\omega_o t - \beta) - R} \qquad (14)$$

In this form, the reflector is assumed to be a point source. If the area of the finite size of the reflector is added in the analysis, then Eq. 13 should be modified as follows:

$$A_{im}(t) = \frac{\pi}{\sin \epsilon(t)}\left[(d(t)\tan(\alpha/2))^2 + \frac{(D_M \cos \psi/2)^2}{4}\right] \qquad (15)$$

where D_M denotes the reflector diameter and ψ denotes the angle between the incoming and reflected sunlight, as shown in Fig. 2. The first term in Eq. 15 can also be expressed in terms of Eq. 14. Even though it will not be considered in this work, the impact of the finite-size of the reflector may not negligible in the energy delivery calculations, especially when the reflector is large and/or at lower altitudes, where the solar image is small. For example, at 1000 km altitude for a polar Earth orbit, where $\psi = 90^o$, the area of the circular solar image at the zenith point

is found 67.93 km^2 from Eq. 13, whereas by using Eq. 15, the same area is equal to 68.33 km^2, i.e., the contribution of the finite size of a 1 km reflector to the area of the solar image is only 0.4 km^2 or approximately 0.5% of the area with the point-mass reflector. Therefore, the finite size of a reflector may be ignored in cases similar to this, but it needs to be evaluated in relation with the orbit altitude and the size of the reflector when large reflectors and/or low altitudes are considered.

The geometric relationships presented in this section will be used to calculate the total energy delivered in the next section.

3. Integral of Delivered Energy

The energy collected by the reflector with area A_M is delivered across an image area $A_{im}(t)$ during an orbital pass. The power density on the ground can be expressed by the following relationship:

$$\sigma_M = I_o \frac{A_M}{A_{im}(t)} \cos \frac{\psi}{2} \tag{16}$$

where σ_M is power density, I_o is the solar constant defined as the mean solar energy per unit area, decreasing by the inverse-square of the distance from the Sun, ψ is defined as the incidence angle between incoming and outgoing sunlight and is fixed in this study due to the dawn/dusk type orbit selected. From Eq. 16, it can be observed that the larger the image is, the lower the power density on the ground. This is why a lower altitude orbit is in principle preferable, as the power density is higher with the smaller image area for a given size of reflector. The penalty for lower altitude orbits is a shorter pass duration as well as increasing perturbations, e.g. atmospheric drag for the Earth, which are out of scope this study. The power received by a ground target with area A_{sf} can then be written as:

$$P_{sf} = \sigma_M A_{sf} = I_o \frac{A_M A_{sf}}{A_{im}(t)} \cos \frac{\psi}{2} \tag{17}$$

Finally, one can determine the total energy delivered by integrating Eq. 17 such that:

$$
\begin{aligned}
E_{sf} &= \int_o^{T_{pass}} P_{sf} \mathrm{d}t = I_o A_M A_{sf} \cos \frac{\psi}{2} \int_o^{T_{pass}} \frac{1}{A_{im}(t)} \mathrm{d}t \\
&= I_o A_M A_{sf} \frac{\cos \psi/2}{\pi(\tan \alpha/2)^2} \int_o^{T_{pass}} \frac{(R+h)\cos(\omega_o t - \beta) - R}{\left(\sqrt{R^2 + (R+h)^2 - 2R(R+h)\cos(\omega_o t - \beta)}\right)^3} \mathrm{d}t
\end{aligned}
\tag{18}
$$

Equation 18 can be analytically solved by using `Mathematica` and the following solution is found after rearranging the result:

$$E_{sf} = I_o A_M A_{sf} \frac{\cos \psi/2}{\pi(\tan \alpha/2)^2} \frac{1}{\omega_o} \left[\frac{F(m|n)}{Rh} - \frac{E(m|n)}{R(2R+h)} - \frac{2(R+h)\sin(\beta - \omega_o t)}{(2Rh + h^2)\sqrt{2R(R+h)(1 - \cos(\beta - \omega_o t)) + h^2}} \right]\Bigg|_0^{T_{pass}} \tag{19}$$

where $F(m|n)$ and $E(m|n)$ are elliptic integrals of first and second kind, respectively. Their parameters m, n are given as

$$m = \frac{\beta - \omega_o t}{2} \tag{20a}$$

$$n = \frac{-4R(R+h)}{h^2} \tag{20b}$$

8

The quantity of solar energy delivered can then be computed within the integral bounds $[0, T_{pass}]$. However, even before solving the integration in Eq. 18, one can infer the energy delivery properties at a given instant during a pass from Eq. 17. Given that the reflector and the ground-target area, as well as the incidence angle are fixed, the only property that determines the energy delivered at each instant of time is the image area. Recall that the solar image starts from being infinitely stretched and reaches to its minimum area at the zenith, before becoming infinitely stretched at the end of the pass. Hence, the power density begins from zero, reaching its maximum before decreasing to zero again.

The above integral in Eq. 18 is presented for an idealised case with no losses, for a flat surface or solar panels on the ground, and assumes that the entire ground target is available for energy reception during a pass. The last assumption may especially be strong and not true for all altitudes if the solar image is not large enough to cover the entire ground target. In the following subsections, this and a number of other non-ideal conditions will be discussed.

3.1. Effective ground-target area

In the ideal case of a circular ground target, such as a solar power farm, there will be a minimum altitude at which the minimum image size at zenith will be exactly the same size as the ground target. From Fig. 1, consider the following relationship for the image diameter at the zenith point as:

$$D_{im} = h \tan \alpha \tag{21}$$

Note that the finite size of the reflector is not included in Eq. 21. The altitude at which the minimum image size would be the same size D_{sf} as the ground target size can then be found as:

$$h_{lim} = \frac{D_{sf}}{\tan \alpha} \tag{22}$$

Note the ground-target diameter D_{sf}, instead of the image diameter D_{im}, is used to find this limiting altitude. Moreover, h_{lim} can also be found by rewriting Eq. 22 in terms of R_{sf} and $\tan \alpha/2$. In that case, it is found that there occurs a slight underestimation of this limiting altitude due to the tangent function, which may be important when optimising the image size for a given ground target. As an example, $h_{lim} = 1074.2$ km for $D_{sf} = 10$ km and $\alpha = 0.0093$ rad from Eq. 22, whereas $h_{lim} = 1074.3$ km for $R_{sf} = 5$ km and $\alpha/2 = 0.00465$ rad, when Eq. 22 is rewritten to define this altitude in terms of the ground target radius, R_{sf} and $\alpha/2$.

The implication of h_{lim} is that, for any altitude $h \geq h_{lim}$, the entire ground target area can be used to receive energy delivered from a reflector spacecraft. On the other hand, when $h < h_{lim}$ a more detailed area relationship must be considered to model the delivered energy more accurately. This relationship can be expressed as:

$$A_{sf}^{eff} = \begin{cases} h \geq h_{lim} & A_{sf} \\ h < h_{lim} & A_{sf}^{eff} \end{cases} \tag{23}$$

where A_{sf}^{eff} is the effective ground target area. As expressed in Eq. 23, $A_{sf}^{eff}(t)$ needs to be evaluated with respect to $A_{im}(t)$ during an orbital pass to calculate the ground-target area that is illuminated. For a reflector spacecraft at an altitude $h < h_{lim}$, three distinct cases can be identified as shown in Fig. 3.
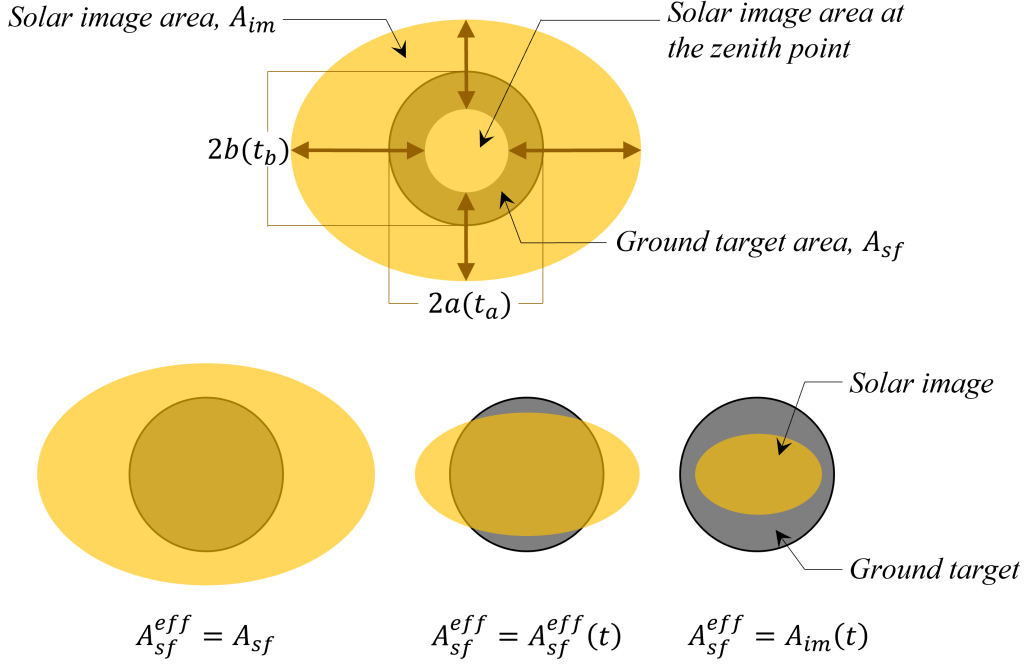
Figure 3: Three distinct cases of the solar image area in relation to the ground target area. Top figure: the solar image is stretched initially and becomes a circle at the zenith point before stretching through the end of orbital pass. At time t_b and t_a, the semi-minor and semi-major axes dimensions of the solar image become equal to the ground target radius, respectively. Bottom figure: Depending on the time during the orbital pass, the effective ground target area changes as the solar image changes during the pass.

At the beginning of the pass, in principle the entire ground target area would be available for energy reception. This is essentially the same case as for $h \geq h_{lim}$, except that it does not hold when the semi-minor of the solar image $b(t)$ is less than the ground-target radius, R_{sf}, after some time t_b, which can be calculated as

$$
\begin{aligned}
R_{sf} = b(t_b) &= d(t_b) \tan \alpha/2 \\
&= \sqrt{R^2 + (R+h)^2 - 2R(R+h) \cos(\omega_o t_b - \beta)} \tan \alpha/2 \\
\Rightarrow t_b &= \frac{1}{\omega_o} \left[\arccos\left(\frac{R^2 + (R+h)^2 - (R_{sf}/\tan(\alpha/2))^2}{2R(R+h)} \right) + \beta \right]
\end{aligned}
\tag{24}
$$

Equation 24 provides t_b after the zenith point, denoted as t_b^f, i.e., when the reflector is descending to the horizon. To calculate t_b before the zenith point, i.e., t_b^0, following expression must be used:

$$
t_b = \frac{1}{\omega_o} \left[\beta - \arccos\left(\frac{R^2 + (R+h)^2 - (R_{sf}/\tan(\alpha/2))^2}{2R(R+h)} \right) \right]
\tag{25}
$$

Note that semi-minor axis $b(t)$ of the solar image may be smaller than R_{sf} at all times depending on the size of the ground target and the orbit altitude, and this phase may never occur.

10

One can also calculate point the time point t_a, at which the semi-major axis of the solar image $a(t)$ is equal to the ground target radius, R_{sf}, as

$$
\begin{aligned}
R_{sf} = a(t_a) &= \frac{d(t_a)^2 \tan(\alpha/2)}{\sin \epsilon(t)} \\
&= \frac{[R^2 + (R+h)^2 - 2R(R+h)\cos(\omega_o t_a - \beta)]\tan(\alpha/2)}{R - (R+h)\cos(\omega_o t_a - \beta)} \\
\Rightarrow t_a &= \frac{1}{\omega_o}\left[\arccos\left(\frac{[R^2 + (R+h)^2]\tan(\alpha/2) - R_{sf}R}{(R+h)[2R\tan(\alpha/2) - R_{sf}]} \right) + \beta \right]
\end{aligned} \tag{26}
$$

The same arrangement in Eq. 25 can be made to find t_a before the zenith point. Once $t \geq t_a$, the solar image would be contained entirely inside the ground target, and the effective ground-target area would equal the image area itself, i.e. $A_{sf}^{eff} = A_{im}(t)$. An important point to note for this phase is that, because the energy is only received via the ground-target area equal to $A_{sf}^{eff} = A_{im}(t)$, the power received by the ground target would be constant and equal to $P_{sf} = I_o A_M \cos\psi/2$, with no other effect considered. Also note that, contrary to t_b, t_a can always be found, as $a(t)$ becomes infinite in the beginning of the pass before decreasing and tending again towards infinity.

In between the t_b and t_a time points, there is a phase where only a portion of the solar image would overlap with a portion of the ground target, with the rest of the image outside the ground-target boundary. This case requires a more detailed effective ground-target area calculation, as the area contained within the ground target is not a simple geometric shape anymore, but is within the intersection of the ground-target boundary and the instantaneous image ellipse, as shown in Fig. 3. If a cartesian axis set is centered at the common origin of the ground-target circle and the image ellipse, the intersecting area can be divided to four equal parts and the intersecting area can be calculated by a combination of elliptical and circular sections in one of those parts. A schematic of this division is shown in Fig. 4. First, the intersection point of the ground-target circle and
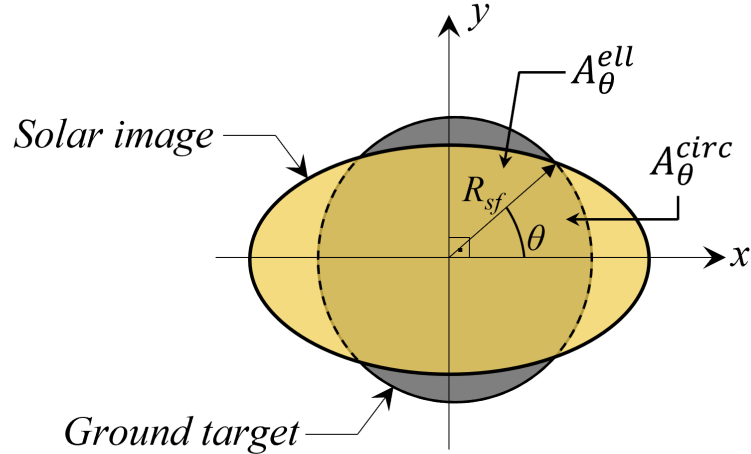

Figure 4: Schematic of intersecting area calculation

the instantaneous image ellipse is found in cartesian coordinates from the mutual solution of the definition of the circle and ellipse, by rewriting both as $y = f(x)$. The intersection point can therefore be found from:

$$\sqrt{x^2 - R_{sf}^2} = \sqrt{\frac{(a(t)b(t))^2 + (b(t)x)^2}{a(t)^2}}$$

$$\Rightarrow x(t) = \frac{\sqrt{(a(t)b(t))^2 + (a(t)R_{sf})^2}}{a(t)^2 - b(t)^2} = \frac{\sqrt{b(t)^2 + R_{sf}^2}}{1 - \left(\frac{b(t)}{a(t)}\right)^2} = \frac{\sqrt{b(t)^2 + R_{sf}^2}}{\cos \epsilon(t)} \tag{27}$$

$$\Rightarrow x(t) = \frac{d(t)\sqrt{[d(t)\tan(\alpha/2)]^2 + R_{sf}^2}}{(R + h)\sin(\omega_o t - \beta)}$$

where the intersection coordinate $y(t)$ can be found by substituting $x(t)$ in the equation defining the circle formed by the ground target. Then, the angle of this point in polar coordinates is calculated as $\theta(t) = \arctan y(t)/x(t)$. Using the fact that the radial distance from the origin equals the ground-target radius at the intersection point, the area of the circular portion defined by angle θ can be found as

$$A_\theta^{circ} = \frac{\theta}{2\pi}\pi R_{sf}^2 = \frac{\theta}{2}R_{sf}^2 \tag{28}$$

The remaining portion of the intersecting area is defined by an elliptical portion of the solar image. The generic formula of the area of an elliptical section can be found by parameterising the ellipse (for the details of the derivation, see Appendix A):

$$A_\theta^{ell} = \frac{1}{2}ab\arctan\frac{a\tan\theta}{b} \tag{29}$$

However, in this problem, the area of the elliptical portion needed is defined by the angle $\pi/2$-$\theta(t)$. Simply substituting $\pi/2$-$\theta(t)$ in Eq. 29 would result in an erroneous area due to the geometry of the ellipse. Instead, the area of the elliptical portion defined by the angle θ must be subtracted from the area of the elliptical portion defined by the angle $\pi/2$ to find the desired area. Note that the latter is equal to the quarter of the area of an ellipse. Then, the following expression can be used to find A_θ^{ell}:

$$\begin{aligned}A_\theta^{ell}(t) &= \frac{\pi a(t)b(t)}{4} - \frac{1}{2}a(t)b(t)\arctan\frac{a(t)\tan\theta(t)}{b(t)} \\ &= \frac{\pi b(t)^2}{4\sin\epsilon(t)} - \frac{b(t)^2}{2\sin\epsilon(t)}\arctan\frac{\tan\theta(t)}{\sin\epsilon(t)}\end{aligned} \tag{30}$$

The sum of the circular and elliptical areas from above expressions then yield a quarter of the total intersecting area contained within the ground-target boundaries. Then, the total area can be

found as:

$$
\begin{aligned}
A_{sf}^{eff}(t) &= 4(A_\theta^{circ}(t) + A_\theta^{ell}(t)) = 4\left[\frac{\theta(t)}{2}R_{sf}^2 + \frac{\pi b(t)^2}{4\sin\epsilon(t)} - \frac{b(t)^2}{2\sin\epsilon(t)}\arctan\frac{\tan\theta(t)}{\sin\epsilon(t)}\right] \\
&= 2\theta(t)R_{sf}^2 + \frac{2b(t)^2}{\sin\epsilon(t)}\left[\frac{\pi}{2} - \arctan\frac{\tan\theta(t)}{\sin\epsilon(t)}\right] \\
&= 2\theta(t)R_{sf}^2 + \frac{2d(t)^3\tan(\alpha/2)}{R - (R+h)\cos(\omega_o t - \beta)}\left[\frac{\pi}{2} - \arctan\frac{y(t)}{x(t)}\frac{d(t)}{(R - (R+h)\cos(\omega_o t_a - \beta))}\right]
\end{aligned}
$$
(31)

As noted earlier, if $b(t)$ is already smaller than the ground target radius at the beginning of an orbital pass, the above expression would then describe the effective ground target area before the solar image is fully contained in the ground target boundaries at t_a.

Finally, after the effective ground-target area expressions for each phase are presented, the following conditions can be defined:

$$
A_{sf}^{eff} = \begin{cases} \pi R_{sf}^2, & t \in [0, t_b^0]; t \in [t_b^f, T_{pass}] \\ \pi a(t)b(t), & t \in [t_a^0, t_a^f] \\ \text{Eq. 31}, & t \in (t_b^0, t_a^0); t \in (t_a^f, t_b^f) \end{cases}
$$
(32)

As a result, the integration presented in Eq. 18 now needs to be separated into three phases with appropriate integration limits in accordance with Eq. 32, with no other effects considered. Because the profile is symmetric, it is in fact sufficient to integrate the appropriate expressions until $T_{pass}/2$ and then multiply by two.

In addition to the areal relationships, the ground-target orientation will also introduce further issues to consider for solar energy delivery from space. This case would be most relevant to tilted photovoltaic panels at a solar power farm, as will be considered next.

3.2. Solar panel tilt

Thus far, the analysis has intrinsically assumed that the ground target is parallel to the local horizontal plane. This is often not the case in real solar farms, where a tilt angle is introduced to optimise the collected solar energy. However, in the case of reflected solar energy during an orbital pass, the tilt angle reduces the effectiveness of the energy delivery. That is to say, even if the reflector spacecraft projects the solar image on ground, after a certain elevation angle, it would project this image to the "back" of the panels. While this does not alter the energy delivered to the ground, the reflected sunlight becomes ineffective as the back of solar panels are generally not designed to transform the solar energy into electricity.

The panel tilt means that there is in fact an effective pass duration, $T_{pass}^{eff} < T_{pass}$, and it is a function of the panel tilt angle. From Fig. 1, T_{pass}^{eff} occurs when the elevation angle $\epsilon(t)$ becomes $\pi - \delta$. Then, the following quadratic equation can be derived to determine when this occurs, i.e., T_{pass}^{eff}:

$$
\epsilon(t) = \pi - \delta = \arccos\frac{(R+h)\sin(\omega_o t - \beta)}{\sqrt{R^2 + (R+h)^2 - 2R(R+h)\cos(\omega_o t - \beta)}}
$$

$$
\Rightarrow \cos(\omega_o t - \beta)^2 - 2\left(\frac{R}{R+h}\right)\cos(\delta)^2\cos(\omega_o t - \beta) + \left[\cos(\delta)^2\left(\left(\frac{R}{R+h}\right)^2 + 1\right) - 1\right] = 0
$$
(33)

If the transformation $q = \cos(\omega_o t - \beta)$ is made, the real roots of Eq. 33 after the transformation can be used to find T_{pass}^{eff} as

$$T_{pass}^{eff} = \frac{1}{\omega_o}[\arccos(q_{1,2}) + \beta] \tag{34}$$

where T_{pass}^{eff} is selected for $0 < T_{pass}^{eff} \leq T_{pass}$ and $\delta \leq 90^o$. The introduction of T_{pass}^{eff} makes the separate cases in the previous subsection further separated depending on which phase T_{pass}^{eff} occurs. The power profile will no longer have symmetry, in at least one of the phases, as long as $\delta > 0$. While the integration itself is the same throughout, each phase needs to be calculated separately before being summed to yield the total delivered energy.

In addition to effective ground-target area and the solar panel orientation, the energy received on the ground will experience further losses due to atmospheric transmission, which is discussed in the next subsection.

3.3. Atmospheric Losses

3.3.1. Transmission losses in the atmospheres

Solar energy passing through the atmosphere experiences scattering, attenuation and absorption before reaching the ground. Whilst the exact expressions for each physical phenomena may be difficult to incorporate into the solar energy delivery integral, it is possible to implement transmission losses in the form of transmission efficiency. One such empirical expression can be found for the Earth from Hottel (1976):

$$\tau(t) = c_0 + c_1 e^{-k \sec(\pi/2 - \epsilon(t))} \tag{35}$$

where $\tau(t)$ is a time-dependent coefficient that describes the transmission efficiency of solar radiation through an atmosphere that is free of clouds. This empirical expression provides a simple and straightforward measure to assess the transmission losses for a given elevation angle, ϵ, hence time t during an orbital pass. The constants c_0, c_1, and k are provided in a table format for different ground-target altitudes from sea level up to 2.5 km with 0.5 km intervals (Hottel, 1976). A set of correction coefficients were also suggested by Hottel (1976) to account for the climatic variations which include tropical, mid-latitude summer and winter, and sub-arctic summer (Hottel, 1976). In this paper, sea-level conditions will be considered without any climate correction. The equation then has the following form:

$$\tau(t) = 0.1283 + 0.7559 e^{-0.3878 \sec(\pi/2 - \epsilon(t))} \tag{36}$$

When specific ground targets are considered, appropriate interpolations can be made from the tables provided in Hottel (1976) according to geographical information, including altitude and climate. Figure 5 shows τ during an orbital pass according to Eq. 36.

The atmospheric loss increases at low elevations due to large slant ranges and gradually decreases until the zenith point, i.e. $\epsilon = 90^o$, where the slant range is minimum. However, even at the zenith point, the transmission efficiency remains at approximately 64%. This value decreases to levels approximately 13% at the beginning and the end of a pass, hence large losses may be expected during solar energy transfer to the ground. According to Hottel (1976), the transmission efficiency improves at locations higher than sea level, but does not exceed 70% (Hottel, 1976). Note also for Eq. 35 and Fig. 5 that the energy lost in transmission can also be used for the calculation of heat *added* to the Earth's atmosphere during solar energy delivery.
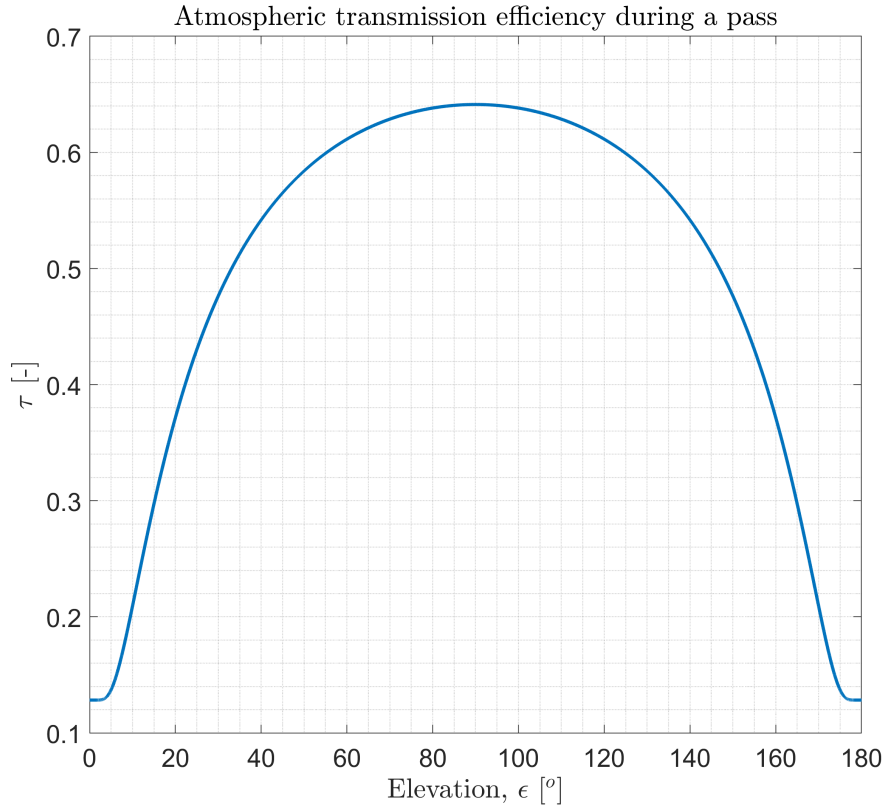
14

Figure 5: Atmospheric transmission efficiency τ during a pass for the Earth.

As for atmospheric transmission losses on Mars, Levine et al. (1977) provides a table of solar radiation at the top of the atmosphere and on ground for Mars for varying atmospheric conditions from clear sky to Martian dust storm (Levine et al., 1977). The transmission efficiency can then be calculated for different regions and is provided as a table for yearly average daily solar radiation (Levine et al., 1977). According to this study, the transmission efficiency is found between 0.7 and 0.85 from poles to equator, respectively. Equatorial regions are envisaged for near-term Martian applications, hence the value 0.85 will be used to scale the energy delivery with no atmosphere for the remainder of the paper.

For the Moon, the transmission is assumed perfect and any other transmission losses due to lunar dust are assumed negligible. When other solar systems objects considered later in the manuscript, the transmission losses will not be taken into account, and solar energy delivery will be considered without any losses.

3.3.2. Cloud cover

Another source of loss in solar energy delivery is cloud cover. To the knowledge of the authors, there is currently no expression that can be used similar to Eq. 35. That is because a model has to incorporate both the global cloud coverage and solar irradiation at the same time, and do so in a way that it can be implemented in the energy integrals presented throughout. However, Canady & Allen (1982), Ehricke (1979), and Ehnberg & Bollen (2005) state that solar illumination in a

cloudy day is no less than the quarter that of a clear day, and no less than the one-third in places partly cloudy on average throughout the year for the Earth (Canady & Allen, 1982; Ehricke, 1979; Ehnberg & Bollen, 2005), at least in the zenith point of a pass. In this study a cloudless sky will be assumed throughout and no losses due to cloud cover will be implemented.

3.4. Final form of the energy integral

The final form of the integral includes the effective ground target area, orientation and atmospheric transmission losses. As discussed earlier, the effective ground target area introduces three different cases. Introduction of the ground target orientation introduces three further cases. Therefore, even though the solution to the energy integral is the same as Eq. 18 throughout, different cases must be considered for each phase. Their sum then yields the total solar energy received. The nine cases are presented as follows:

- $T_{pass}^{eff} > t_b^f$

$$
E_{sf} = I_o A_M \cos(\psi/2)
\begin{cases}
\frac{A_{sf}}{\pi(\tan\alpha/2)^2} \left[\int_0^{t_b^0} \tau(t) \frac{1}{A_{im}(t)} dt + \int_{t_b^f}^{T_{pass}^{eff}} \tau(t) \frac{1}{A_{im}(t)} dt \right], & t \in [0, t_b^0]; t \in [t_b^f, T_{pass}^{eff}] \\[2ex]
\int_{t_a^0}^{t_a^f} \tau(t) dt, & t \in [t_a^0, t_a^f] \\[2ex]
\frac{2}{\pi(\tan\alpha/2)^2} \int_{t_b^0}^{t_a^0} \tau(t) \frac{A_{sf}^{eff}(t)}{A_{im}(t)} dt, & t \in (t_b^0, t_a^0); t \in (t_a^f, t_b^f)
\end{cases}
\tag{37}
$$

- $t_a^f < T_{pass}^{eff} < t_b^f$

$$
E_{sf} = I_o A_M \cos(\psi/2)
\begin{cases}
\frac{A_{sf}}{\pi(\tan\alpha/2)^2} \int_0^{t_b^0} \tau(t) \frac{1}{A_{im}(t)} dt, & t \in [0, t_b^0] \\[2ex]
\int_{t_a^0}^{t_a^f} \tau(t) dt, & t \in [t_a^0, t_a^f] \\[2ex]
\frac{1}{\pi(\tan\alpha/2)^2} \left[\int_{t_b^0}^{t_a^0} \tau(t) \frac{A_{sf}^{eff}(t)}{A_{im}(t)} dt + \int_{t_a^f}^{T_{pass}^{eff}} \tau(t) \frac{A_{sf}^{eff}(t)}{A_{im}(t)} dt \right], & t \in (t_b^0, t_a^0); t \in (t_a^f, T_{pass}^{eff}]
\end{cases}
\tag{38}
$$

- $T_{pass}^{eff} < t_a^f$

$$
E_{sf} = I_o A_M \cos(\psi/2)
\begin{cases}
\frac{A_{sf}}{\pi(\tan\alpha/2)^2} \int_0^{t_b^0} \tau(t) \frac{1}{A_{im}(t)} dt, & t \in [0, t_b^0] \\[2ex]
\int_{t_a^0}^{t_a^f} \tau(t) dt, & t \in [t_a^0, T_{pass}^{eff}] \\[2ex]
\frac{1}{\pi(\tan\alpha/2)^2} \int_{t_b^0}^{t_a^0} \tau(t) \frac{A_{sf}^{eff}(t)}{A_{im}(t)} dt, & t \in (t_b^0, t_a^0)
\end{cases}
\tag{39}
$$

16

The above nine cases are presented for the sake of completeness. However, in most practical situations, some of the cases presented can be discarded. For Earth-based solar energy applications, the solar panel tilt angle δ is no greater than 45° (Jacobson & Jadhav, 2018), therefore the cut-off in T_{pass} is likely to occur through the end of the pass at most low Earth orbit altitudes. This implies that Eqs. 38 and 39 can be ignored while Eq. 37 is solved. Furthermore, if the reflector altitude is high enough, such that $h > h_{lim}$, then the entire ground-target area would be available for solar energy delivery, reducing the number of equations to be solved to just one, i.e. Eq. 18. It is indeed possible today, or in the future, that some solar energy applications at the Earth and for other planetary bodies require higher tilt angles, lower or higher altitude orbits. The above equations would then provide the complete set of solutions.

4. Selected applications

4.1. Solar energy delivery from polar orbits at the Earth

Terrestrial solar energy generation is restricted to daylight hours due to the rotation of the Earth. The most prominent application of orbiting reflectors is therefore to extend the utilisation hours of solar farms on the Earth. This extension may be considered for the dawn/dusk period of each day, which is critical in terms of energy consumption, where demand is high but solar energy supply is low (Fraas, 2012; Fraas et al., 2013). An orbiting solar reflector placed on a polar orbit along the day/night terminator line could provide additional solar power to offset the drop in supply. Such an orbit would ideally be a Sun-synchronous orbit, tracking the Sun throughout the Earth's orbit around the Sun and free of eclipses. If the same ground target is to be illuminated, repeating ground-track orbits may also be considered.

In this paper, a circular polar orbit around the Earth perpendicular to the equator at 1000 km altitude is analysed for simplicity and conciseness. The Earth's radius is taken as 6378.2 km and its gravitational parameter μ as 3.986×10^5 km^3/s^2. As the orbit plane is perpendicular to the incoming sunlight, the reflector attitude is pitched at 45°, such that $\psi = 90^o$. During the pass it is assumed that the reflector tracks the ground target, although the pitch angle relative to the Sun remains fixed. In addition, this case study considers a 1 km diameter reflector and the ground target is a 10 km diameter circular solar farm whose panels are tilted at $\delta = 15^o$. The comparison is made with a case where during the pass there is no loss in atmospheric transmission, the entire solar farm area is available for energy reception and the solar panels are parallel to the ground. The delivered power profile is then presented in Fig. 6.

At 1000 km altitude, a reflector would have an orbit period $T = 105$ min and $T_{pass} = 1057.4$ sec or 17.6 min. At $\delta = 15^o$, only 850.8 sec would be effectively used for solar energy reception at the solar power farm. This may seem a modest loss, but it is 15% of the total available pass duration, and eventually further decreases the total energy delivered. During this effective pass duration, the reflected solar image is larger than the solar farm most of the time (blue dotted line), and is contained within the farm boundaries (yellow dotted line) after a brief period where a portion of the solar image illuminates a portion of the solar farm (red dotted line). The total energy delivered, E_{sf}, as the area under the curve, equals 0.0350 GWh. If $\delta = 0$, E_{sf} would be 0.0352 GWh. Although this difference is small, a slight increase in the tilt angle would result in a much higher loss in the delivered energy as the profile is exponential-like before and after the zenith point.

The contrast with the no-loss case is stark. In the case where there are no losses considered, the total deliverable energy is exaggerated by the absence of atmospheric losses and the availability of
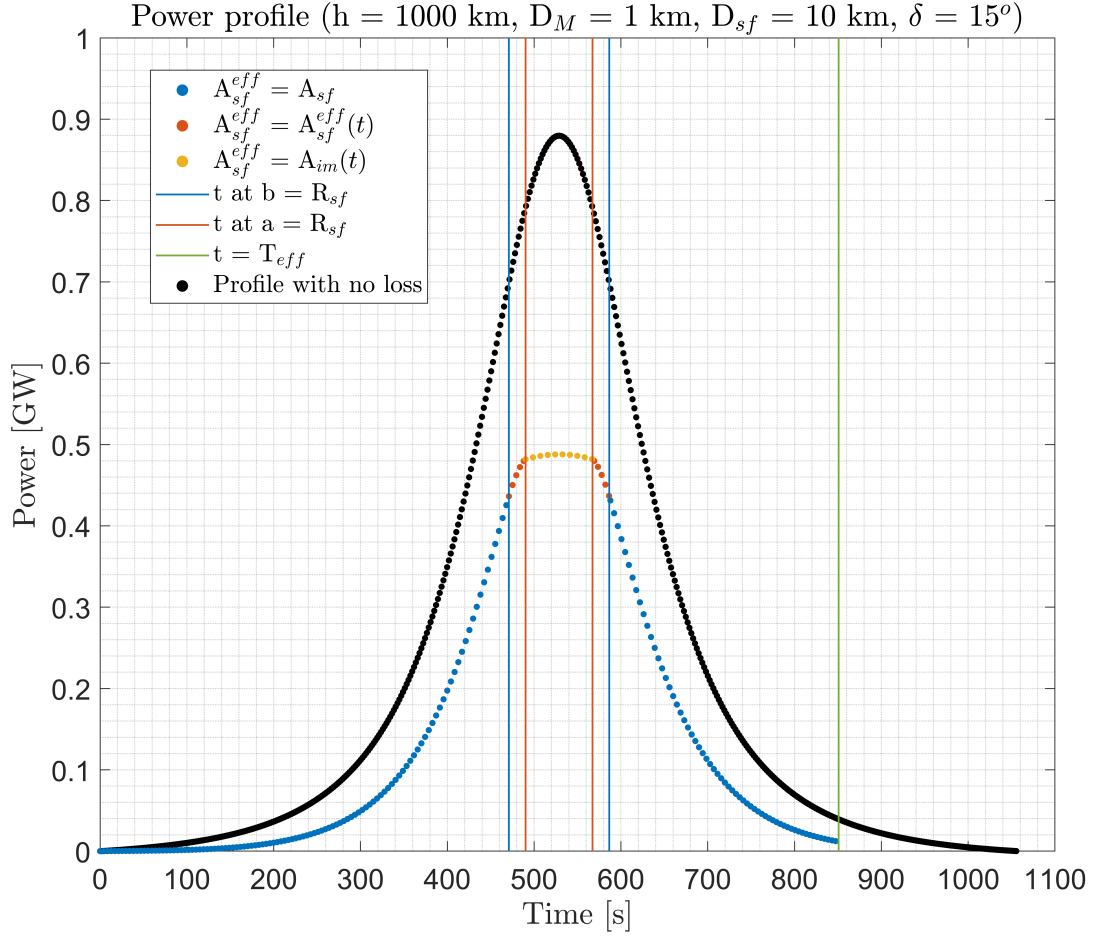
Figure 6: Delivered solar power profile from a 1000-km polar orbit around Earth. The diameters of reflector and solar farm are 1 km and 10 km, respectively. Solar panel tilt is 15°.

the entire solar farm at all times. The total delivered energy in this case is equal to 0.063 GWh, i.e. 1.8 times the value calculated with losses. It may also be considered for simplicity that all of the solar image area is available for energy reception. In that case, $A_{im}(t) = A_{sf}$, therefore the delivered energy equals $E_{sf} = I_o A_M (\cos \pi/4) T_{pass}$ from Eqs. 17 and 18. The delivered energy would then be $E_{sf} = 0.223$ GWh, or more than 6 fold of the delivered energy with losses. While all of the image area would be available for nighttime illumination applications, the finite size of the solar farm must be considered in electricity generation applications.

The most relevant comparison with the literature may be made with Fraas (2012). In Fraas (2012), the authors consider a 10 km diameter reflector spacecraft at a 1000-km circular polar sun-synchronous orbit (Fraas, 2012). The authors then provide the delivered energy from a single spacecraft to a 10-km diameter solar farm. No panel tilt is implemented in Fraas (2012). For the validity of the point-mass reflector approximation in the calculation of the solar image size, the results in Fraas (2012) are adapted in this study for a 1 km diameter reflector. Table 1 shows a comparison of Fraas (2012) and this study.

Table 1: Delivered energy comparison between Fraas (2012) and this study for a 1 km diameter reflector at a 1000 km polar orbit

Study	Losses	Effective ground area	Delivered energy during a pass [GWh]
Fraas (2012)	Slant range losses, fixed $\sim 25\%$	Fixed	0.161
This study	Atmospheric transmission, variable during a pass	Variable	0.0352

As seen in Table 1, Fraas (2012) introduces a loss factor called "slant range losses," which the authors use as a source of loss that decreases the power density (Fraas, 2012). It is not clear whether slant range losses are intended for losses due to a stretched elliptical solar image or both for the stretched image and the atmospheric losses. To the understanding of this paper's authors, it is intended for areal losses and not for atmospheric losses. The value of 25% is calculated from the solar power density values (ideal and with losses) given in Fraas (2012). If the power density at the Earth is multiplied by the circular ground target area according to Eq. 17, it is understood that Fraas (2012) finds that 0.549 GW of solar power is constantly delivered to the ground at each instant of an orbital pass with a 1 km diameter reflector (the actual value is 54.9 GW with a 10 km diameter reflector). Recall that the orbital pass duration at a 1000 km circular orbit is 17.6 min, or 0.29 h. Then the total delivered energy to the ground would be 0.161 GWh in Fraas (2012). Under the same assumptions of the reflector, ground target and orbit sizes, the energy delivered is found to be 0.0352 GWh in this study. The value found in Fraas (2012) is ~ 4.6 times more than that of this study. The overestimation appears to result from both the omission of atmospheric losses and the variable area relationships. The power delivered is extremely low at low elevations which seems to be ignored in Fraas (2012). Combined with atmospheric transmission losses, which themselves are also higher at low elevations, the discrepancy between this study and Fraas (2012) study can be seen, which also underscores the importance of higher fidelity modelling.

In addition to terrestrial applications, one may also consider speculative reflected solar energy applications at different solar system objects, especially the Moon and Mars, which will be investigated in the next section.

4.2. Non-terrestrial solar energy delivery

4.2.1. Energy delivery to different solar system objects

It may also be desirable to utilise solar energy for a number of applications, not only for the Earth but also for the Moon, Mars or potentially for other planetary bodies. These applications may be for providing additional solar energy to future crewed and robotic exploration missions, for water extraction at the lunar poles or simply for illumination purposes to extend surface operation hours, as well as long-term applications such as terraforming Mars. In the Moon's case, the absence of an atmosphere means no transmission losses and potentially extremely low altitude (or periapsis) orbits, which, in turn, translates as high solar power density due to a smaller solar image size. Similarly, the thinner atmosphere of Mars allows lower altitude orbits and a smaller solar image, despite the low solar flux due to its distance from the Sun. For both the Moon and Mars, their smaller sizes and gravitational parameters mean that for a given altitude, the orbit period, hence the pass duration, is longer compared to the orbits around the Earth, as shown in Fig. 7. This may allow more energy to be delivered for a given altitude.
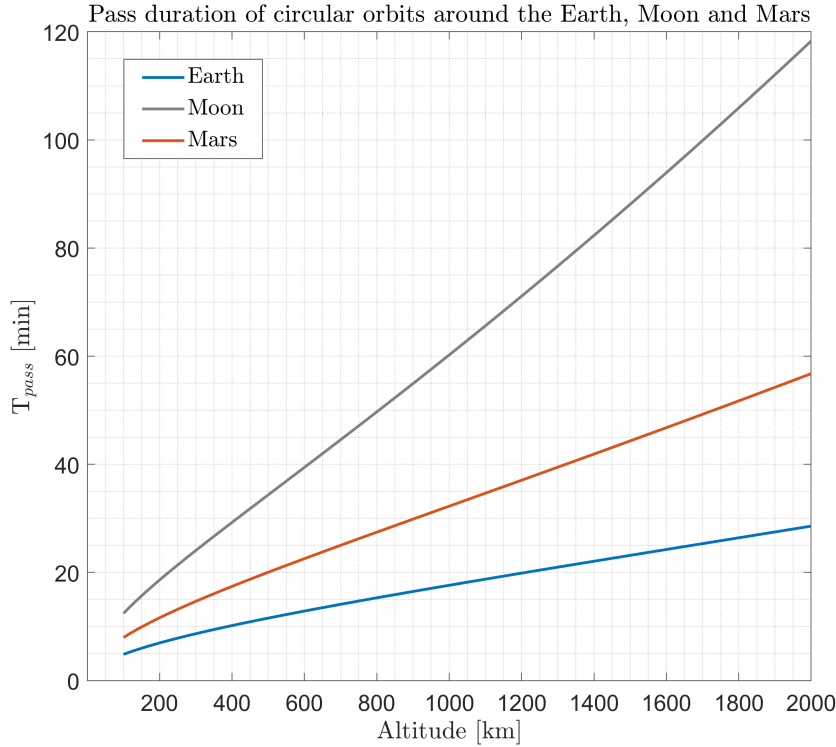
19

Figure 7: Orbital pass duration at circular orbits around the Earth, Moon and Mars.

In this case study, solar energy delivery from a range of circular orbit altitudes will first be investigated for the Moon and Mars in comparison with the Earth. For the Moon, the radius R and the gravitational parameter μ are equal to 1738 km and 4.9×10^3 km^3/s^2. The solar constant and the solar angle α are assumed the same as that of the Earth with no atmosphere for the Moon. As for Mars, $R = 3389.9$ km, $\mu = 4.28 \times 10^4$ km^3/s^2 and the average distance to the Sun $\rho_{sun} = 1.52$ AU, whereas the solar constant and the solar angle α reduce to 0.598 GW/km^2 and 0.0062 rad, respectively.

First, the total energy collected by a 1 km diameter reflector and reflected onto the ground will be calculated at a given range of altitudes between 100 and 2000 km. Note from the previous subsection that, when the entire solar image is considered, Eq. 17 simplifies as $E_{sf} = I_o A_M (\cos \pi/4) T_{pass}$, in an idealised case with no atmospheric losses. Here, the energy delivery is calculated both with and without atmospheric losses and is presented in Fig. 8.

The results show a large difference between the Moon and the Earth and Mars, and similar values between the Earth and Mars. These results may at first seem counter-intuitive. The significant energy delivered for the lunar case can in part be accounted for by the absence of an atmosphere. However, given the fact that especially Mars is farther from the Sun, hence the solar constant is less than half of that of for the Earth and the Moon, one might expect energy delivery at Mars to be much lower than for the Earth, not similar. But in fact it can even be higher than on the Earth if atmospheric effects are included.

The result is driven by a combination of parameters. Assuming the idealised case with no

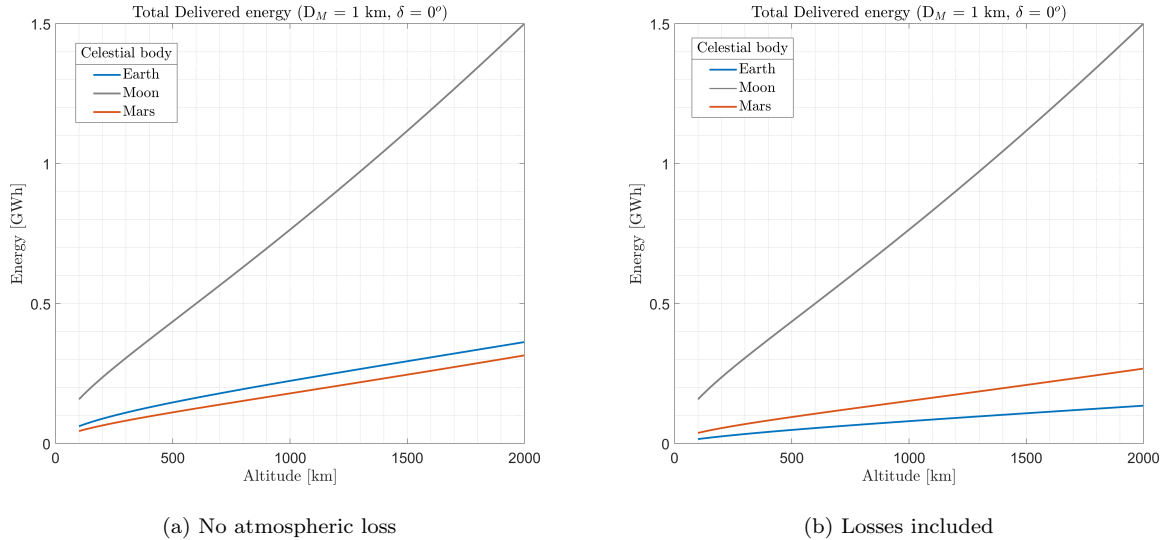| | (a) No atmospheric loss | (b) Losses included |

Figure 8: Delivered energy for a range of altitudes at Earth, the Moon and Mars, with and without atmospheric losses

atmosphere, the parameters that drive the energy delivery are the solar constant I_o and the pass duration, T_{pass}, from Eq. 18. The former is scaled with the inverse square of the distance from the Sun, whereas the latter is a function of the size and mass of the celestial body, from Eqs. 1 and 2. When all the constant terms are ignored, the energy delivered is scaled with the following coefficient, κ:

$$\kappa = \frac{1}{\rho_{sun}^2}\sqrt{\frac{(R+h)^3}{M}}\beta = \frac{1}{\rho_{sun}^2}\sqrt{\frac{(R+h)^3}{M}}\arccos\frac{R}{R+h} \tag{40}$$

It can be seen that κ includes the distance to the Sun, orbit period and the angle β. If a length unit is defined as the distance between the Earth and the Sun, $LU = 1$ AU, or 1.496×10^8 km, and a mass unit as the mass of the Earth $MU = M_E$, then κ can be used as a non-dimensional indicator of the reflected solar energy delivered at different celestial bodies.

As an example, one could consider a 1000 km altitude to compare different cases. Note from Fig. 8a that the energy delivered for the Earth, Moon and Mars are 0.223, 0.764, and 0.179 GWh, respectively, when no atmospheric loss is considered. For the Earth, then, κ is equal to 1.824×10^{-7}. On the other hand, κ is 6.234×10^{-7} and 1.438×10^{-7} for the Moon and Mars, respectively, in nondimensional units. The ratio for the κ values between celestial bodies is equal to the ratio between the energy delivered to each body when atmospheric losses are not considered. If the κ values are normalised with the κ value of the Earth, then the values become 1, 3.41, and 0.788 for the Earth, the Moon and Mars and a more intuitive comparison can be made. In its non-dimensional form, κ then allows for a simple scaling and a relative comparison between different celestial bodies.

The indicator κ can then be utilised to assess solar energy delivery at a number of planetary bodies that may be of interest for future exploration missions. Figure 9 presents the κ values normalised with the Earth's κ value for all the solar system planets, Jovian moon Europa, Saturnian moons Titan and Enceladus, the asteroid Ceres and the dwarf planet Pluto. The planetary bodies are selected to represent some of the past and future space missions to these.
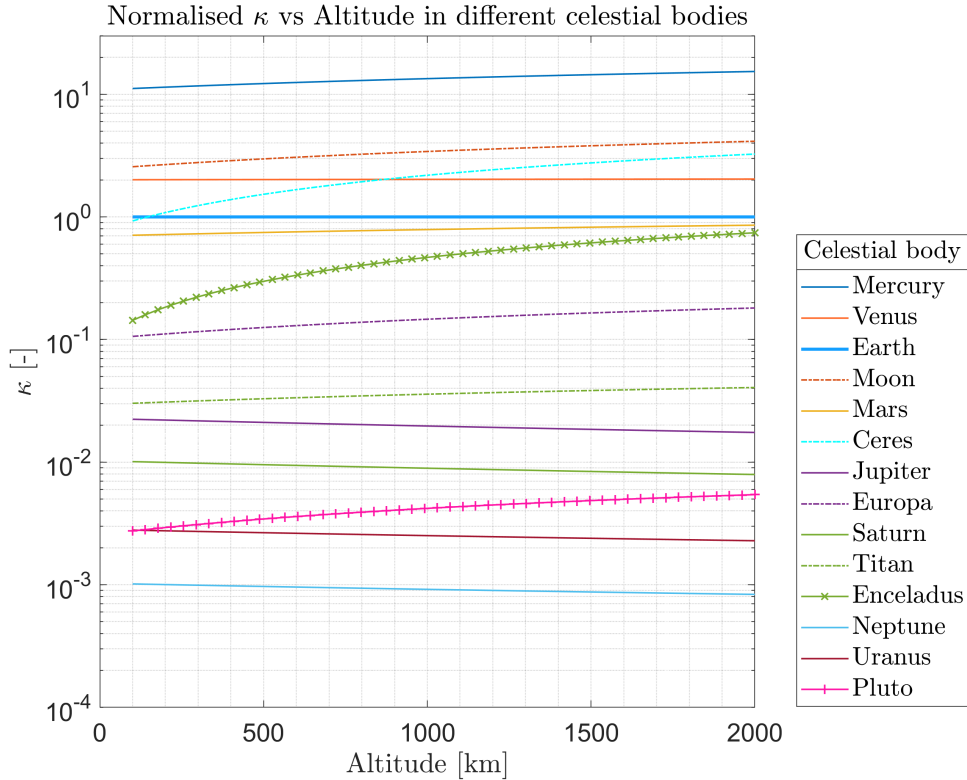
Figure 9: κ value for a number of solar system bodies and different reflector altitudes.

From Fig. 9, note that the Earth as $\kappa = 1$. With Mercury being the closest to the Sun and a relatively small object, the reflected solar energy is the highest. However, some of the results shown in Fig. 9 are not as intuitive and immediately apparent. The second highest, for instance, is not Venus but the Moon, in which it appears that the proximity of Venus to the Sun cannot compensate for short duration orbital passes. Another potentially interesting result is for Ceres, which has lower delivered energy at the lowest altitude (100 km) than the Earth but increases gradually, surpassing both the Earth and Venus after approximately 900 km altitude. For Enceladus, despite its large distance from the Sun, energy delivery is similar to that of Mars and the Earth at 2000 km altitude. Similarly, the energy delivered is higher for Pluto, the farthest object considered in this analysis (∼40 AU), than Uranus and Neptune, which is due to its small size and low mass and hence long duration orbit passes.

In this section, the general case of solar energy delivery at different solar system objects has been investigated and their scalability discussed. One of the specific non-terrestrial solar energy applications is for lunar night-side illumination to enable and/or extend crewed and robotic exploration activities. This will be discussed in the next section.

4.2.2. Lunar night-side illumination

It may also be desirable to use reflected solar energy to enhance the lunar surface operations by providing illumination. This type of application was considered for the Earth in the 1970s and early 1980s (Rush, 1977; Ehricke, 1979; Canady & Allen, 1982). As discussed in the previous

subsection, orbital passes around the Moon are longer for a given orbit altitude than those at the Earth due to the smaller size of the Moon. Combined with the absence of an atmosphere, more solar energy can be delivered to a surface site during a single pass for the same size of reflector at the same altitude.

The level of solar illumination before atmospheric transmission losses is determined to be 128,000 lux on the Earth (IES Calculation Procedures Committee, 1984). The illumination is likely to be in this order for the Moon, as well, if reflected light from the Earth is ignored. In order to determine the level of illumination on the surface, the following relationship is adopted:

$$\sigma_{lx} = I_{lx}\frac{A_M}{A_{im}}\cos\frac{\psi}{2} \tag{41}$$

Equation 41 is the same as Eq. 16 except that the solar constant I_o and power density, σ_M, are replaced by their equivalent in lux, I_{lx} and σ_{lx}, again assuming an ideal flat reflector. In this way, the illumination levels can be compared with some known reference levels on the Earth. The reflector is again assumed pitched at 45°, such that $\psi = 90^o$. First, the illumination profile is investigated for a 1000 km altitude orbit around the Moon with reflectors sized between 20 m and 1 km, as presented in Fig. 10.
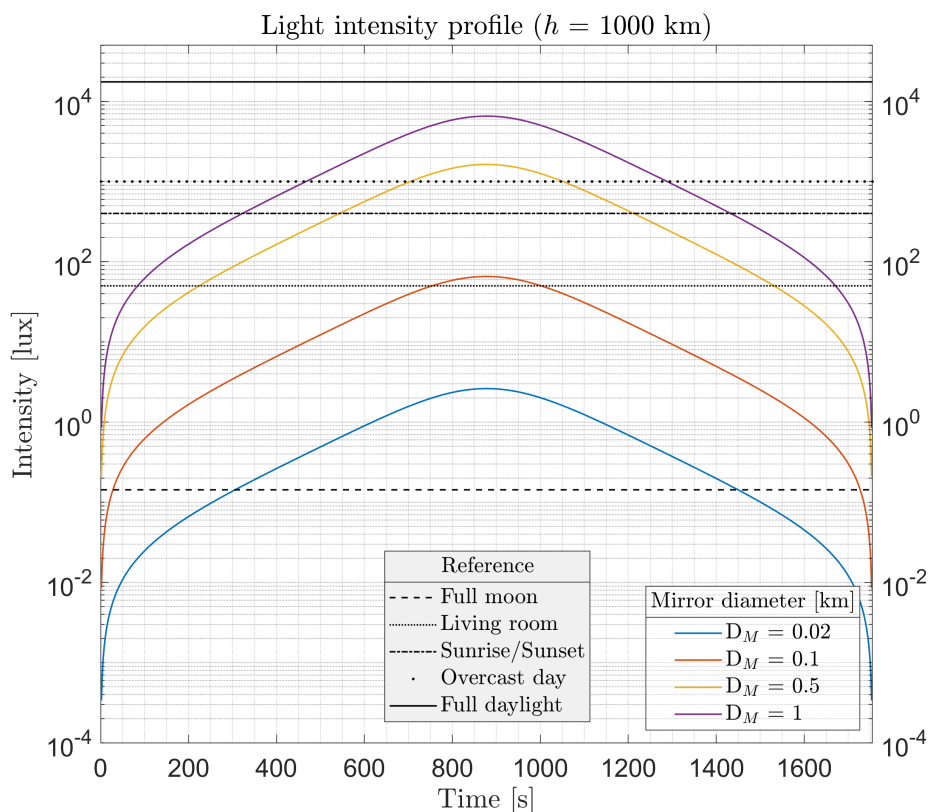

Figure 10: Variation in illumination on the lunar surface during an orbital pass.

Note that the pass duration at this altitude is 30 min. The reference illumination values are

23

for the illumination on the Earth[1]. The illumination is extremely low in the beginning of a pass, increasing rapidly before decreasing again. The illumination never reaches average full daylight conditions (17500 lux) at this altitude, although it reaches the level of an overcast day (1000 lux) for 1 km and 500 m sized reflectors. If smaller reflectors are to be considered, the illumination level is on the order or below living room conditions (50 lux (Pears, 1998)), and for most of the pass it is higher than full-moon-level (0.143 lux (Canady & Allen, 1982)) illumination on the Earth. The auditorium level illumination ($\sim$1 lux) is considered sufficient to read a newspaper with normal eyesight, whereas low streetlight ($\sim$2 lux) is considered sufficient for slow driving with little traffic (Canady & Allen, 1982). It then appears that the peak illumination levels achieved by a 20 m reflector may be sufficient for certain tasks on the Moon, although a 100 m reflector may be more desirable.

The results presented in Fig. 10 can be extended to a range of altitudes for peak illumination. In this case, orbit altitudes between 100 and 2000 km are considered and the light intensity at the zenith point (i.e., $\epsilon = 90^o$) is calculated. The results are presented in Fig. 11.
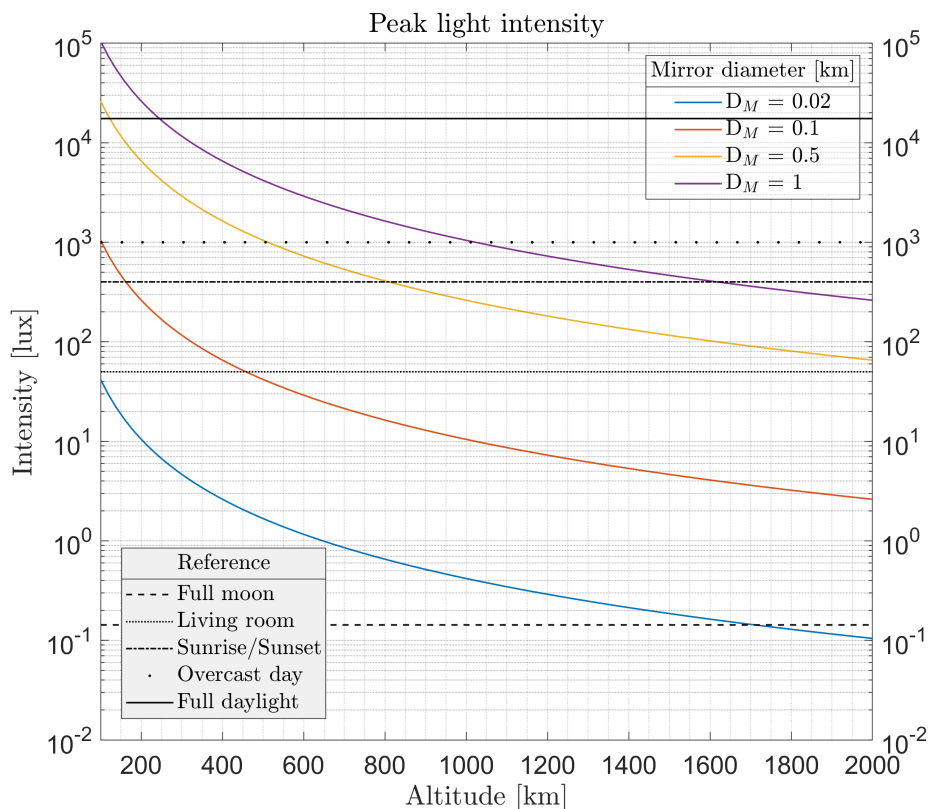

Figure 11: Peak light intensity on lunar surface from reflectors at different altitudes

In this case, both peak illumination levels higher than full daylight and lower than full-moon can

---

[1] The reference illumination values for sunrise/sunset, overcast day and full daylight are obtained from "Radiometry on photometry on astronomy" at `http://stjarnhimlen.se/comp/radfaq.html\#10`. Accessed on June 16, 2021.

be observed at the lowest and the highest altitudes, respectively. The trade-off for a given reflector size with altitude is between high illumination and short pass duration or low illumination and long pass duration. Note that to achieve living room illumination condition as a reference working conditions for astronauts, reflectors must be larger than 100 m in diameter. At this lower boundary, the altitude must also be lower than 500 km. This level of illumination can always be achieved by a reflector 500 m or larger in diameter. Alternatively, a train of reflectors may be considered at a very low lunar orbit with the smallest size reflector necessary to achieve near living room conditions.

The results in this section suggest that orbiting solar reflectors can be used for lunar illumination applications to support crewed and uncrewed operations. Alternatively, the reflectors can also be used to supply the energy needs in future lunar and Martian endeavours, not only for night-side but also day-side and polar regions, which is discussed in the next subsection.

4.2.3. Solar energy delivery to a fixed sized ground-target on the Earth, Moon and Mars

Another case study in this section is the energy delivered to a fixed 1 km diameter ground target with no panel tilt for a potential human outpost with a single 1 km reflector. The total energy delivered on ground will be compared again for the Earth, Moon and Mars. Applications include enhancing solar power generation on the surface of the Moon or Mars, where the Earth is presented for reference. The results are shown in Fig. 12.
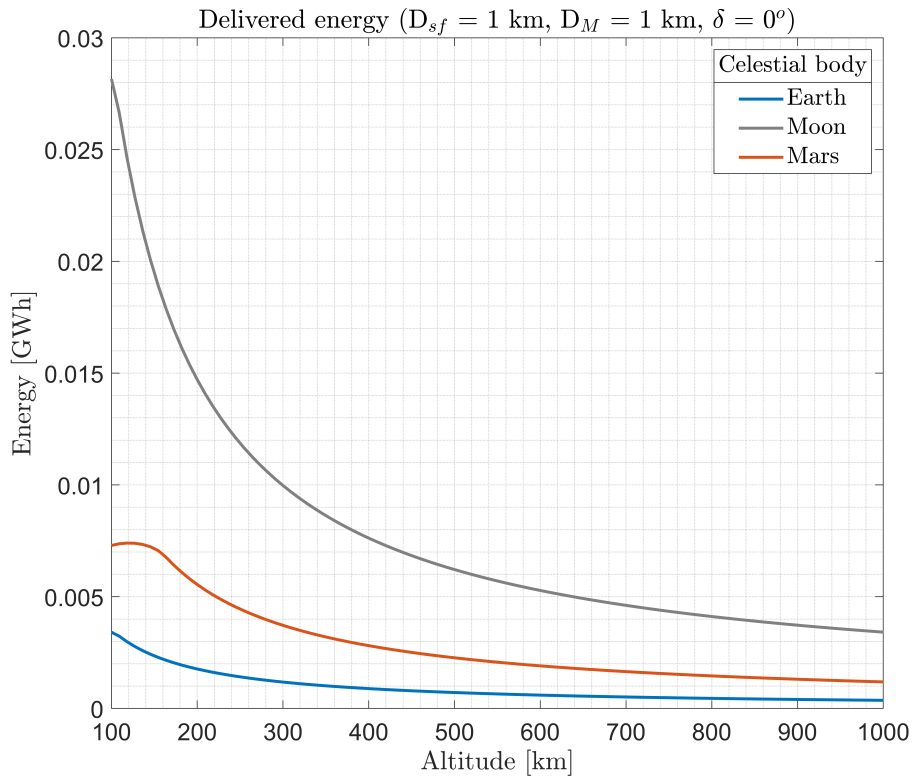

Figure 12: Energy received at a 1 km diameter area on ground at the Earth, the Moon and Mars.

The solar energy delivered to a 1 km diameter target on the Moon and Mars is always higher

25

than that for the Earth. In the Moon's case, the difference results from the absence of atmospheric losses and a much longer pass duration for the same altitude with respect to the Earth, again due to its much smaller size and gravitational parameter, from Eq. 2 and as shown in Fig. 7. Note for both the Moon and Earth that an optimum altitude is not reached for the range of altitudes considered in the analysis (i.e., 100-1000 km), which occurs at approximately 80 km at the Moon, and at a slightly higher altitude (but below 100 km) for the Earth. In the case of Mars, despite the low solar flux, the smaller angle α results in a smaller image size, which, combined with the longer pass duration at a given altitude (as shown in Fig. 7), allows more efficient use of the given 1 km diameter target for energy reception. In fact, an optimum altitude is available at which approximately 7.5 MWh energy can be received. Combined with more efficient atmospheric transmission, as well as a longer pass duration due to the smaller size and gravitational parameter with respect to the Earth, solar energy delivery to the Martian surface appears more efficient than for the Earth surface at all times. Relevant to this latter point, the results presented in Fig. 12 have the following implication. A reflector whose size is smaller than 1 km can be used in the lunar environment to evaluate the effectiveness of a 1 km size reflector for terrestrial applications. In either case, employment of orbiting solar reflectors in the lunar environment would allow not only supplying energy and illumination on the surface of the Moon, but also tests orbiting solar reflectors for the Earth and potentially Mars.

5. Conclusion

In this paper, an analytical model for solar energy delivery to a stationary ground target from an ideal flat reflector in a circular orbit has been presented. The idealised form of energy transfer has a closed form analytical solution using elliptic integrals. Moreover, a higher fidelity model incorporates varying solar image area, fixed ground target size and solar panel orientation, as well as atmospheric transmission losses to calculate the energy delivered accurately for different applications. The final integral expression for the energy delivered has multiple discrete cases depending on the characteristics of the application. The case study presented for a terrestrial application demonstrates the importance of higher fidelity modelling as opposed to the simplified calculations previously used in the literature. A subsequent case study for solar energy delivery at the Earth, Moon and Mars shows that the energy delivered can be scaled with a simple scaling parameter. The results also suggest that the employment of orbiting solar reflectors in the lunar environment may be strategically useful to obtain insights into the usefulness of the reflectors for all three planetary bodies for future applications.

Appendix A. Area of an elliptical section

The area of an elliptical section defined by the angle θ is found by parameterising the ellipse with inner and outer circles, whose radii are the ellipse semi-minor and semi-major axes with

dimensions b and a, respectively, as shown in Fig. A.1.
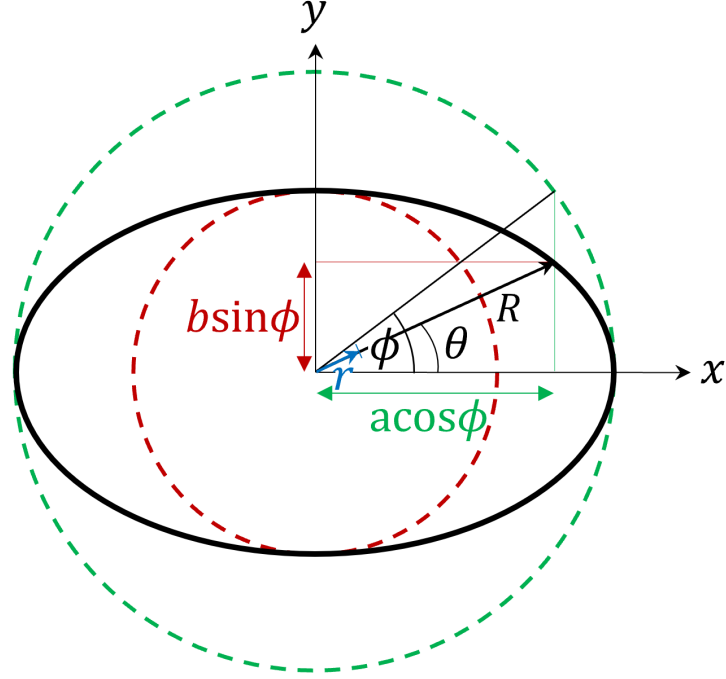

Figure A.1: Parameterisation of an ellipse with inner and outer circles

If a cartesian axis set is centered at the origin of the ellipse and the circles, the x and y coordinates of the point on the ellipse described by angle θ can be written as:

$$
\begin{aligned}
x &= a \cos \phi \\
y &= b \sin \phi
\end{aligned}
$$
(A.1)

where ϕ is an auxiliary angle defined by the associated circle. The angle θ can then found by trigonometry:

$$
\tan \theta = \frac{b \sin \phi}{a \cos \phi}
$$
(A.2)

The angle ϕ can be found as a function of θ by rearranging the above equation:

$$
\phi = \arctan \frac{b \tan \theta}{a}
$$
(A.3)

Before substituting ϕ into Eq. A.1, note the following trigonometric half-angle relationships:

$$
\begin{aligned}
\cos 2\phi &= \frac{1 - (\tan \phi)^2}{1 + (\tan \phi)^2} \\
\sin 2\phi &= \frac{2 \tan \phi}{1 + (\tan \phi)^2}
\end{aligned}
$$
(A.4)

27

If $\cos 2\phi = 2\cos^2\phi - 1$ and $\sin 2\phi = 2\sin\phi\cos\phi$, rearranging and substituting the above equations yields

$$\cos\phi = \frac{1}{\sqrt{1+(\frac{a\tan\theta}{b})^2}}$$
$$\sin\phi = \frac{\frac{a\tan\theta}{b}}{\sqrt{1+(\frac{a\tan\theta}{b})^2}} \tag{A.5}$$

Then, substituting the above equations in Eq. A.1 yields

$$x = \frac{a}{\sqrt{1+(\frac{a\tan\theta}{b})^2}}$$
$$y = \frac{a\tan\theta}{\sqrt{1+(\frac{a\tan\theta}{b})^2}} \tag{A.6}$$

The area of an ellipse by integration in polar coordinates can be expressed as follows:

$$
\begin{aligned}
A &= \int_0^u \int_0^R r\,\mathrm{d}r\,\mathrm{d}\theta \\
&= \frac{1}{2}\int_0^u R^2\,\mathrm{d}\theta = \int_0^u x^2 + y^2\,\mathrm{d}\theta \\
&= \frac{1}{2}\int_0^u \Big[\frac{a^2}{1+(\frac{a\tan\theta}{b})^2} + \frac{(a\tan\theta)^2}{1+(\frac{a\tan\theta}{b})^2}\Big]\mathrm{d}\theta \\
&= \frac{1}{2}\int_0^u \frac{\mathrm{d}\theta}{\frac{\sin^2\theta}{b^2}+\frac{\cos^2\theta}{a^2}}
\end{aligned} \tag{A.7}
$$

where r denotes the length of an infinitesimally small bounded segment at the elliptical region defined by angle θ, R is distance from the center of the ellipse at a given angle θ defined as $R(\theta) = \sqrt{x^2+y^2}$, and the upper bound u of the integral denotes the polar angle measured from the x-axis that the area of the portion of ellipse is calculated. The integration in Eq. A.7 eventually yields

$$A = \frac{1}{2}ab\arctan(\frac{a\tan u}{b}) \tag{A.8}$$

Note that for the integral bounds $[0, 2\pi]$, the integration in Eq. A.7 yields $A = \pi ab$, i.e. the area of an ellipse. More relevant to this study, the area of the elliptical portion defined by $\pi/2$ can be found by setting the upper bound $u = \pi/2$, which equals the quarter of the area of an ellipse, $A = \frac{\pi}{4}ab$.

References

Bewick, R., Sanchez, J. P., & McInnes, C. R. (2011). Use of orbiting reflectors to decrease the technological challenges of surviving the lunar night. In *62nd International Astronautical Congress (IAC 2011)* (pp. 1597–1609). Cape Town, South Africa: IAF volume 2. Paper no. IAC-11-A5.1.11.

Billman, K. W., Gilbreath, W. P., & Bowen, S. W. (1977). *Introductory assessment of orbiting reflections for terrestrial power generation*. Technical Report NASA-TM-73230 NASA.

Bonetti, F., & McInnes, C. (2019). Space-enhanced terrestrial solar power for equatorial regions. *Journal of Spacecraft and Rockets*, *56*, 33–43.

Buckingham, A. G., & Watson, H. M. (1968). Basic concepts of orbiting reflectors. *Journal of Spacecraft and Rockets*, *5*, 851–854.

Canady, J. E., & Allen, J. L. (1982). *Illumination from space with orbiting solar-reflector spacecraft*. Technical Report NASA-TP-2065 NASA.

Ehnberg, J. S., & Bollen, M. H. (2005). Simulation of global solar radiation based on cloud observations. *Solar Energy*, *78*, 157–162.

Ehricke, K. A. (1979). Space light: space industrial enhancement of the solar option. *Acta Astronautica*, *6*, 1515–1633.

Fraas, L. M. (2012). Mirrors in space for low-cost terrestrial solar electric power at night. In *38th IEEE Photovoltaic Specialists Conference* (pp. 2862–2867). Austin, TX: IEEE.

Fraas, L. M., Landis, G. A., & Palisoc, A. (2013). Mirror satellites in polar orbit beaming sunlight to terrestrial solar fields at dawn and dusk. In *2013 IEEE 39th Photovoltaic Specialists Conference (PVSC)* (pp. 2764–2769). Tampa, FL: IEEE.

Gillespie, D., Wilson, A. R., Martin, D., Mitchell, G., Filippi, G., & Vasile, M. (2020). Comparative analysis of solar power satellite systems to support a moon base. In *71st International Astronautical Congress (IAC 2020)*. Online: IAF. Paper no. IAC-20,C3,4,2,x59999.

Giorgini, J. D. (2015). Status of the JPL Horizons Ephemeris System. In *IAU General Assembly*. volume 29.

Hottel, H. C. (1976). A simple model for estimating the transmittance of direct solar radiation through clear atmospheres. *Solar energy*, *18*, 129–134.

IES Calculation Procedures Committee (1984). Recommended practice for the calculation of daylight availability. *Journal of the Illuminating Engineering Society*, *13*, 381–392.

Jacobson, M. Z., & Jadhav, V. (2018). World estimates of pv optimal tilt angles and ratios of sunlight incident upon tilted and tracked pv panels relative to horizontal panels. *Solar Energy*, *169*, 55–66.

Leary, W. E. (1993). Russians to test space mirror as giant night light for earth. *The New York Times* [online], (p. 1). Available at: www.nytimes.com/1993/01/12/science/russians-to-test-space-mirror-as-giant-night-light-for-earth.html [Accessed 23 June 2021].

Levine, J. S., Kraemer, D. R., & Kuhn, W. R. (1977). Solar radiation incident on mars and the outer planets: Latitudinal, seasonal, and atmospheric effects. *Icarus*, *31*, 136–145.

Lior, N. (2013). Mirrors in the sky: Status, sustainability, and some supporting materials experiments. *Renewable and Sustainable Energy Reviews*, *18*, 401–415.

McInnes, C. R. (2009). Mars climate engineering using orbiting solar reflectors. In *Mars* (pp. 645–659). Springer.

Oberth, H. (1929). Methods of space travel. *Munich, Oldenburg*, (p. 494).

Pears, A. (1998). Chapter 7: Appliance technologies and scope for emission reduction. *Strategic Study of Household Energy and Greenhouse Issues. Australian Greenhouse Office*, (p. 61).

Potter, S., & Davis, D. (2009). Orbital reflectors for space solar power demonstration and use in the near term. In *AIAA SPACE 2009 Conference & Exposition*. Pasadena, CA: AIAA.

Rush, W. F. (1977). An orbiting mirror for solar illumination at night. *Solar Energy*, *19*, 767–773.